Conduction mode laser welding with beam shaping using a deformable mirror

Yongcui Mi [a],[*], Satyapal Mahade [a], Fredrik Sikström [a], Isabelle Choquet [a], Shrikant Joshi [a], Antonio Ancona [a],[b]

[a] *Department of Engineering Science, University West, 461 86 Trollhättan, Sweden*
[b] *Physics Department, University of Bari, Via Amendola 173, 70126 Bari, Italy*

ARTICLE INFO

ABSTRACT

This study explores the possibility of tailoring the fusion zone in conduction mode laser welding using a deformable mirror for beam shaping of multi-kilowatt continuous wave laser sources. Three power density distributions were shaped and used in bead on plate welding of Ti64 plates in conduction mode at three travel speeds. The effect on melt pool free surface geometry, cross section, microstructure and hardness profiles was measured and studied. It is shown that the geometry of the melt pool can be modified using a deformable mirror. A narrower and longer melt pool or a wider, shorter and shallower one were indeed obtained forming Gaussian-elliptical power density distributions oriented along and transverse to the travel direction, respectively. The latter distribution could be a favourable option for laser beam additive manufacturing as it could improve process efficiency while reducing remelting of the previous layer. This system has also a promising potential for adaptive process control since it could change fundamentally the beam shape at a rate faster than 10 ms.

1. Introduction

The industrial demand to increase productivity and robustness of continuous wave (cw) high-power laser processes such as welding (LBW) and additive manufacturing (LBAM) requires the industry to progress these technologies beyond current state of the art of flexible automation and control. Currently, the most common control strategies for theses processes are based on controlling the laser power level [1–3], the travel speed [4] and the feedstock feeding rate [5] when using filler metals. Increased flexibility requires the controllable parameters' space to be expanded to deal with different challenges and meet various processing conditions and at the end product requirements. For instance, in LBW of electronic connections, the joints area (interconnection point) is of high importance. A wider and shallower weld with quite high aspect ratio (fusion zone width/depth) is needed due to strength and electrical conductivity requirements. In LBW of butt joints, a wider weld waist is required to minimize the risk of sidewall lack of fusion [6]. However, LBW usually produces narrow welds. In addition, in both LBW and LBAM, the cooling rate is fast due to the low local heat input, which could result in unfavourable microstructures. For example, LBW of Ti64 can have a cooling rate between 100 and 1000 °C/s and the

microstructures produced can be entirely martensitic [7], with low ductility.

Researchers have been looking for different approaches to control the above mentioned processes. Tailoring the beam power density distribution has been recognized as a promising solution, since it directly governs the response of the material to the heat input. The process of redistributing the beam power density is named as beam shaping [8]. By an adaptive beam shaping, it is possible to tailor the beam power distribution both spatially and temporally. In LBW and LBAM, beam shaping could enable a modification of the heat input, and influence melting and solidification behaviour [9,10]. Associated research development efforts and application have shown its potential in dealing with issues in dissimilar materials welding [11], butt joint welding [12], macrostructure and microstructure in LBW and LBAM [13,14] as well as process efficiency [15].

It is found in the literature, that the most common beam shaping devices in LBW and LBAM are scanner mirrors [16–19], which are mainly galvanometric- or piezo-actuators driven. With this beam shaping method, it is possible to achieve oscillation patterns from one-dimensional to three-dimensional. Depending on the driving method, the oscillation frequency can be up to 10 kHz [16]. The drawback of this

---

beam shaping technology is that the oscillation frequency needs to be carefully selected to meet different application requirements. In addition, the processing speed is then slowed down due to the limitation in oscillation speed of the beam. The second approach that has been used for beam shaping in LBW and LBAM is through the use of diffractive optical elements (DOE) that include diffractive beam shapers, diffractive beam diffusers and diffractive beam splitters [20], diffractive holographic optical elements [21] as well as customized optics [22]. One of the common problems of this method is that the flexibility of beam shaping is limited. Another method used for beam shaping recently is through an optical delivery fiber double cladding technology, which couples two variable power levels into the core and the inner cladding of a double clad delivery fiber. It has been applied with both fiber laser and thin-disk solid-state laser [23,11]. For instance, Rinne et al. [11] shaped the beam using a double cladding fiber to investigate the weldability of steel-copper dissimilar lap joints. With this beam shaping technology, the beam profile can be varied, but the beam pattern is predetermined by the fiber structure. This beam shaping method works efficiently for the applications such as high reflective materials welding and gear wheel welding [23]. There are few research efforts that used an adaptive optical element to shape the beam in CO_2 LBW [24,25]. While the applied adaptive optical element has certain flexibility, the control of the device is still limited to the radius of curvature of its surface.

One can conclude from all this that there is a strong potential in a beam shaping method that could expand the space defined by the limitations of all the above mentioned technologies and meet various application requirements in cw high power laser processing. This work presents a new beam shaping technology for a multi-kilowatt cw laser based on a newly designed deformable mirror consisting of piezoelectric actuators directly bonded to a high reflective flexible glass membrane. The deformable mirror does not require water cooling and enables to shape the multi-kilowatt laser beam through a suitably developed closed loop control system. Bead-on-plate conduction mode welding on Ti64 plates with three beam power density distributions and three welding travel speeds has been performed to preliminarily evaluate this beam shaping technology. The effect of beam shaping on melt pool free surface geometry, cross section, microstructure and hardness profiles are presented.

2. Experimental setup and procedure

The welding equipment consisted of a water cooled high power ytterbium-doped fiber laser, a CNC gantry, fixtures, a vision system and an adaptive optics system for beam shaping. The experimental procedure description includes process parameter description and the method used for analyzing the welds.

2.1. Adaptive beam shaping system

The adaptive beam shaping system was integrated into the processing tool from Permanova Lasersystem AB, directly after the beam collimator unit, as shown in Fig. 1. The collimated beam having a diameter of around 20 mm impinged on a deformable mirror that did not require any water cooling. The deformable mirror, from Dynamic Optics s.r.l., was composed of a thin glass flexible membrane pushed and pulled by 19 piezoelectric actuators. The membrane was coated with a high reflectivity (R > 99.99% at 1070 nm) and low absorptivity ($< 10^{-5}$) dielectric coating. Besides reducing laser beam power losses along the optical chain, such an extremely low absorption of the dielectric coating significantly reduced heating of the deformable mirror glass substrate during long exposure at the high-power laser levels. Even though the heat conductivity of glass is worse than other materials such as silicon or silicon carbide [26], a glass substrate was preferred for the fabrication of the DM. To reduce the heat induced deformation the glass membrane was fabricated with fused silica and the piezo actuators were covered with fused silica end caps. Therefore, when the system starts heating the
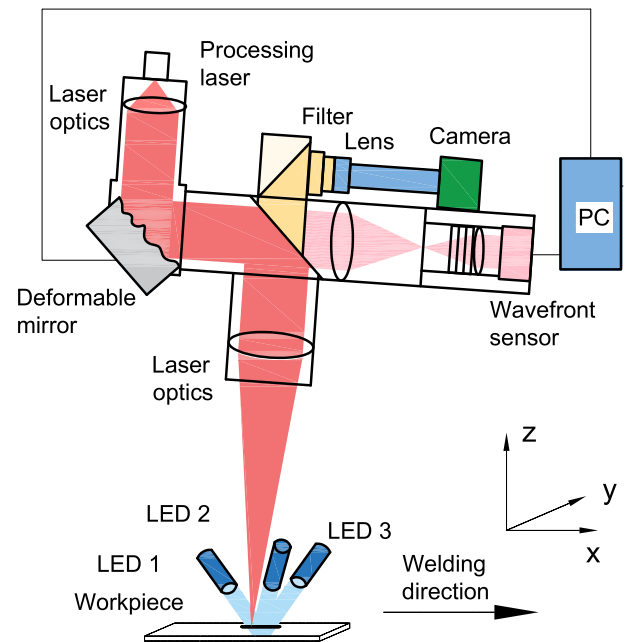

Fig. 1. Components arrangement of the welding setup.

thermal induced deformation on the deformable mirror is very small because of the low coefficient of thermal expansion of quartz and controllable by the closed loop system with a very small use of the actuators dynamic range.

The actuators were disposed in two concentric oval rings to match the beam size with an angle of incidence of 45 degrees. The stroke of each actuator was ± 5 μm. After being folded by the deformable mirror, the laser beam was reflected by a dichroic mirror towards the focusing optics of the processing tool. Behind the dichroic mirror, and opposite to the deformable mirror, a Shack-Hartmann wavefront sensor with 300 μm lens pitch and focal length 4 mm was placed that captured the beam leakage from the dichroic mirror in order to measure in real time the wavefront distortions introduced by the deformable mirror. The deformable mirror was used in closed loop with the wavefront sensor using an integrative controller [27–29]. Based on the wavefront measurement, the adaptive optics closed loop control system developed by Dynamic Optics srl [29] allowed to shape the deformable mirror in real time by acting on the piezoelectric actuators. In the present work, once the beam shape was selected and the piezoelectric actuators were set accordingly, it was kept during the entire process. Therefore, the role of the closed loop control was to maintain the desired beam shape for the whole process. However, the system has the potential to adapt on-the-fly the beam shape to varying process conditions at a rate faster than 10 ms. Preliminary functional tests of the DM were conducted by exposing it at 2-kW for more than 30 min and it was verified that the wavefront and the beam shape did not change, thus indicating that any heating causing a thermal drift of the actuators was within the stroke of the actuators in order to be compensated by the integrative controller [29].

2.2. Welding equipment

The LBW setup is shown in Fig. 2. The laser beam, with a wavelength of 1070 nm, was generated by a 6 kW IPG system (mod. YRL-6000-S) and guided to the processing tool through a 200 μm core diameter optical fiber. The tool, comprised a f = 76 mm collimator and a f = 400 mm focusing lens. It was manipulated by a CNC gantry from Isel® Germany (mod. M40). To avoid back reflections into the optics the tool was mounted on to the gantry with an inclination in the travel direction at an angle of 5° with respect to the workpiece. Shielding gas Argon was provided by a nozzle, as shown in Fig. 2.
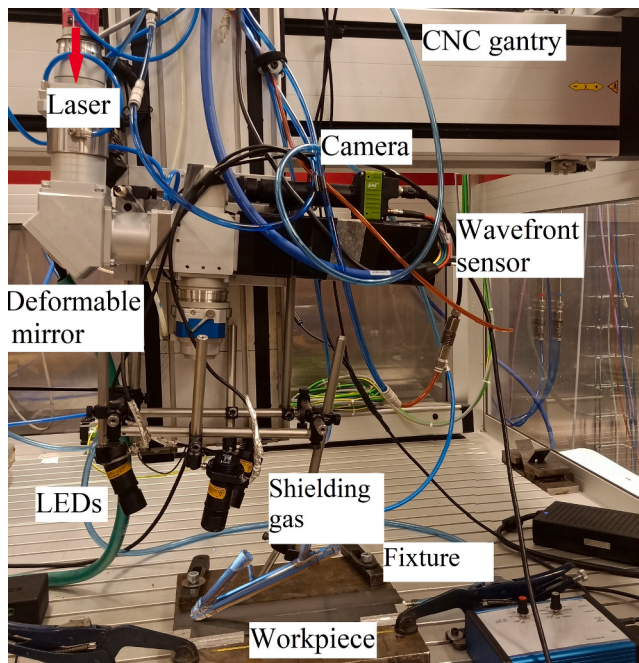
Fig. 2. Welding setup.

Table 1
Parameters of the beam profiles.

Beam profile	Rx (mm)	Ry (mm)	Ry/Rx	Beam area (mm^2)
C	0.72	0.78	1.00	2.10
TE	0.77	1.23	1.60	4.28
LE	0.88	0.66	0.75	2.18

along the x (and y) direction and the beam area. The x-axis was aligned with the travel direction. The beam spot area as shown in Fig. 4 was defined as the region embracing 86% of the total power [31]. This area was delimited by a power density isocontour at a value depending on the beam shape. For the C, TE and LE beam shapes its isovalue was 80.2, 21.7 and 80.6 W/mm^2, respectively.

In a preliminary test the beam shaping system was kept running continuously for half an hour at 2 kW laser power (with a peak power density slightly above 8 kW/cm^2) to test its performance. Next, bead on plate conduction mode welding at 1 kW power was conducted on alloy Ti64 plates with dimensions of 300.0 mm × 40.0 mm × 3.2 mm. The length of each weld was 50 mm. Totally, nine cases were performed that differ through the welding parameters summarized in Table 2.

2.4. Weld bead analysis

Cross cuts of the weld beads were sectioned at a distance of 20 mm from the start using a slow speed, linear precision saw and the sectioned specimens were hot mounted in epoxy resin using an automatic mounting press. The mounted specimens were subjected to standard metallographic procedure programmed specifically for titanium-based alloys to obtain a scratch-free, mirror finished surface. The polished specimens were etched using Barker's reagent (98 ml H$_2$O + 2 ml HBF4). Light optical microscope at lowest possible (5x) magnification was employed for microscopic analysis. The micrographs were stitched together to capture the entire weld geometry in order to measure the different features such as the width. The polished specimens were also analyzed by scanning electron microscope (SEM) (HITACHI TM3000, Japan) to reveal their microstructure at higher magnification.

An automated micro-indentation equipment (Duramin-40, Struers, Denmark) was employed to measure the hardness profile on Vickers scale along the width and depth of the welds. A load of 500 mg was used and the dwell time was kept at 20 s. The hardness profile was measured across the width of the FZ, at a distance of 60–80 μm from the bead surface to avoid the influence of epoxy mount if the indents were too close to the bead surface. The distance between two successive indents was kept at 100 μm (> 3 times the diagonal length of indents) in order to avoid the work hardening effect. A vertical line profile passing approximately through the centre of the FZ towards the base metal (BM) was used to estimate the FZ depth.

3. Results

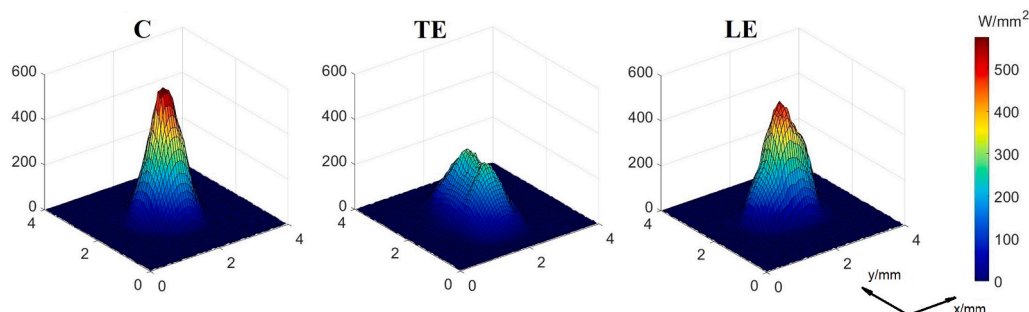This section presents the evaluation of the influence of different

A vision system was used to capture and measure at the workpiece top surface the melt pool free surface. It consisted of a camera (SP5000M-CX4, from JAI), an imaging lens with f = 150 mm and a hard-coated band pass filter (center wavelength at 450 nm and full width at half max of 40 nm), that had been integrated coaxially in the tool. With this configuration the resolution of the vision system was around 14 μm. The vision system was calibrated following Zhang's camera calibration method [30] with a measuring uncertainty of around 2μm, which was determined by the re-projecting error from the image points to world points. Three LEDs were mounted to illuminate the region of the welding melt pool. The exposure time was 100 μs and the acquisition frame rate was 100 frames/s. The width and height of the images were 640 × 512 pixels.

2.3. Welding parameters

Fig. 3 visualizes the power density distributions of the three beam profiles investigated. These distributions were obtained by the deformable mirror system described in Section 2.1 and measured by a Primes GmbH beam profiler. The first one is a Gaussian distribution (hereafter referred to as C), the second power distribution is a transverse elliptical Gaussian (TE) with the major axis perpendicular to the welding direction, while the third is a longitudinal elliptical Gaussian (LE) with the major axis parallel to the welding direction. Table 1 summarizes parameters characterising these profiles, including the radii Rx (and Ry)
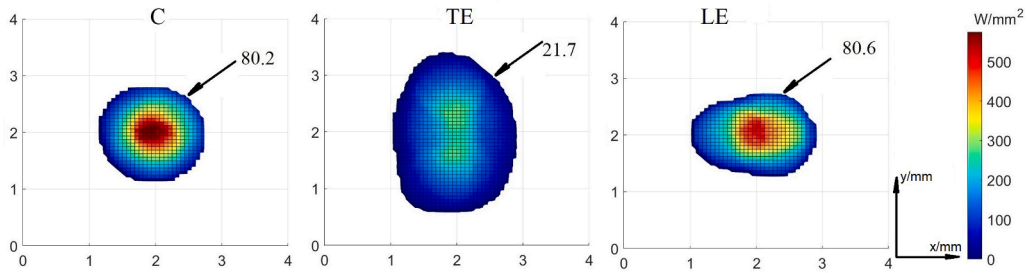

Fig. 3. Measured power distributions.

Fig. 4. Beam areas of the distributions.

Table 2
Welding parameters that differentiate the test cases.

Travel speed (mm/s)	5.0			7.5			10.0		
Power distribution	C	TE	LE	C	TE	LE	C	TE	LE
Test No.	1	2	3	4	5	6	7	8	9

beam profiles. It includes melt pool free surface geometry, fusion zone width measured from cross sections and hardness profiles.

3.1. Melt pool free surface visualization and measurement

Fig. 5 shows for each test case a top view image of the melt pool at the quasi-steady state. Although it is difficult to clearly distinguish the boundary between the melt pool and the solidified bead, it can still be seen that the different beam power density distributions result in significantly diverse melt free surface geometries. It can also be seen that, regardless of the travel speed, the front of the melt pool produced with the TE beam shape is wider and shows smoother curvature changes than for the pools obtained with the other beam shapes. Since it was difficult to identify the melt pool rear edge from the acquired images, in order to evaluate the free surface dimension along the welding direction, a region around the melt pool rear part was histogram-equalized to enhance the contrast. All the acquired images of the fully developed melt pool were used to estimate its free surface contour. The image processing and melt pool contour estimation procedures adopted here were similar to those presented in a previous study [32].

Fig. 6 presents, for each beam profile, the beam power density distribution and the outer contour of the melt pool free surface estimated at the different travel speeds. It can be seen that for each condition the pool front geometry reproduces the beam spot shape. This front is ahead of the spot at $U_{laser} = 5.0$ mm/s. It moves closer to the spot as the travel speed is increased. The TE melt pool is approximately as wide as its beam spot. On the other hand the C and LE pools are always wider than their respective beam spots. Instead, the geometry of the pool rear edge does not reproduce the rear shape of the spot. This difference is more pronounced with the TE profile. With the sharper C and LE profiles it can also be seen that the rear contour of the pool free surface changes proportion when the travel speed is increased. This is more pronounced with the LE profile.

Fig. 7 compares at each travel speed the free surface contours estimated at the different beam profiles. It shows that at the lowest travel speed the differences between the three power density distributions reflect very little in the geometry of the melt pool, apart from the slightly wider front shoulders observed with the TE shape. When the travel speed is increased it can be seen that the TE and LE melt pool contours increasingly differ compared to the C-contour. Using the C-contour at same travel speed as reference, the relative width of the TE melt pool indeed increases when the travel speed is increased while its relative length is almost constant. Inversely, the relative width of the LE melt pool shows little variation when the travel speed is increased while its relative length is increased.

Fig. 8 gives the width and length of the free surface measured from the estimated melt pool contours. The measurement uncertainty was evaluated to be ± 0.05 mm in each case apart from the C and LE profiles at $U_{laser} = 10.0$ mm/s for which it was ± 0.1 mm. The uncertainty was determined by the estimated standard deviation of the width measurement shown in Fig. 9. The quantitative comparison shows a melt pool width about 7% wider with the power density distribution TE compared to C at the travel speed $U_{laser} = 7.5$ mm/s and 12% wider at $U_{laser} = 10.0$
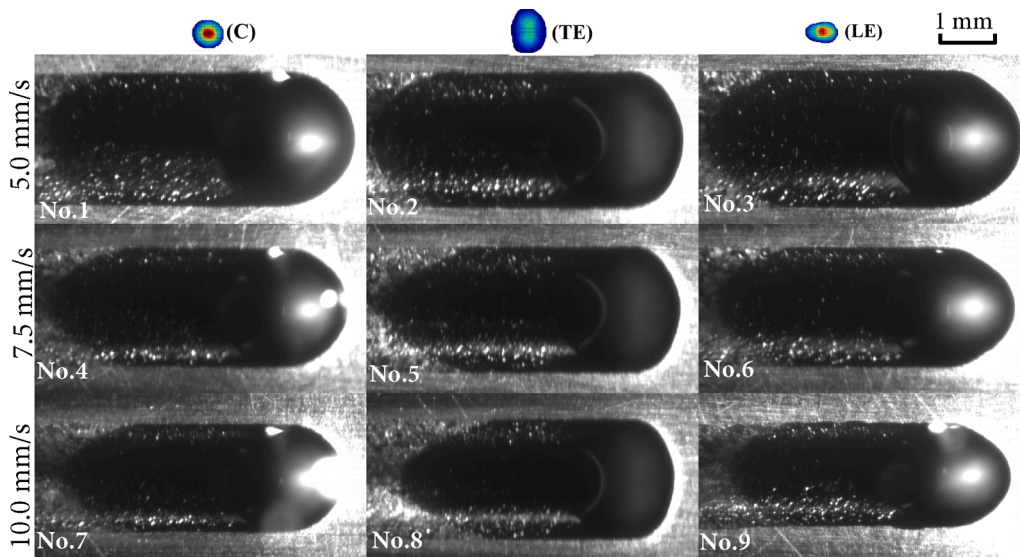

Fig. 5. Top-view images of the fully developed melt pool for the different test cases defined in Table 2.
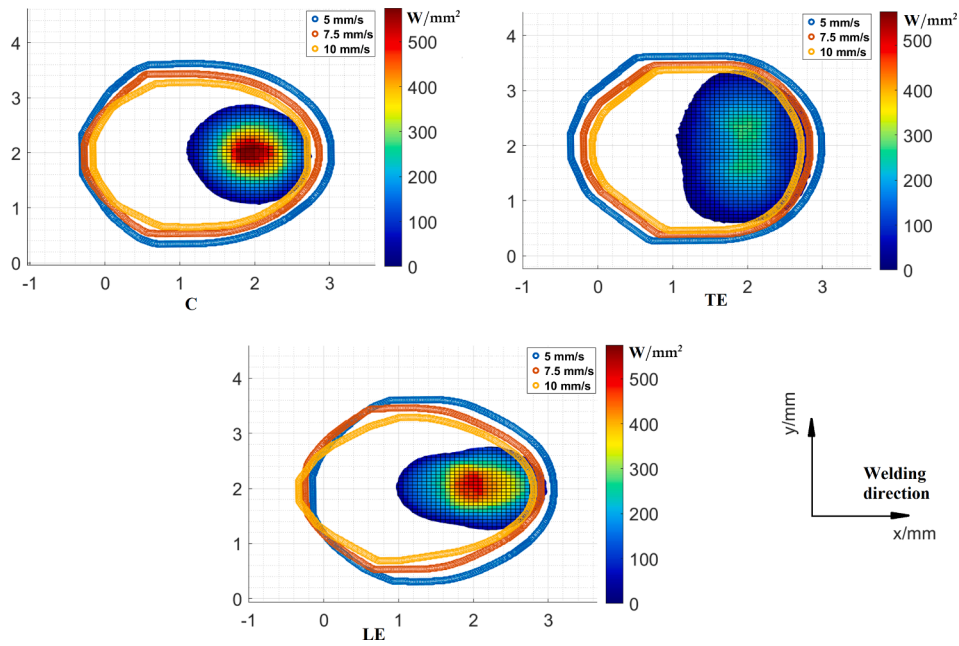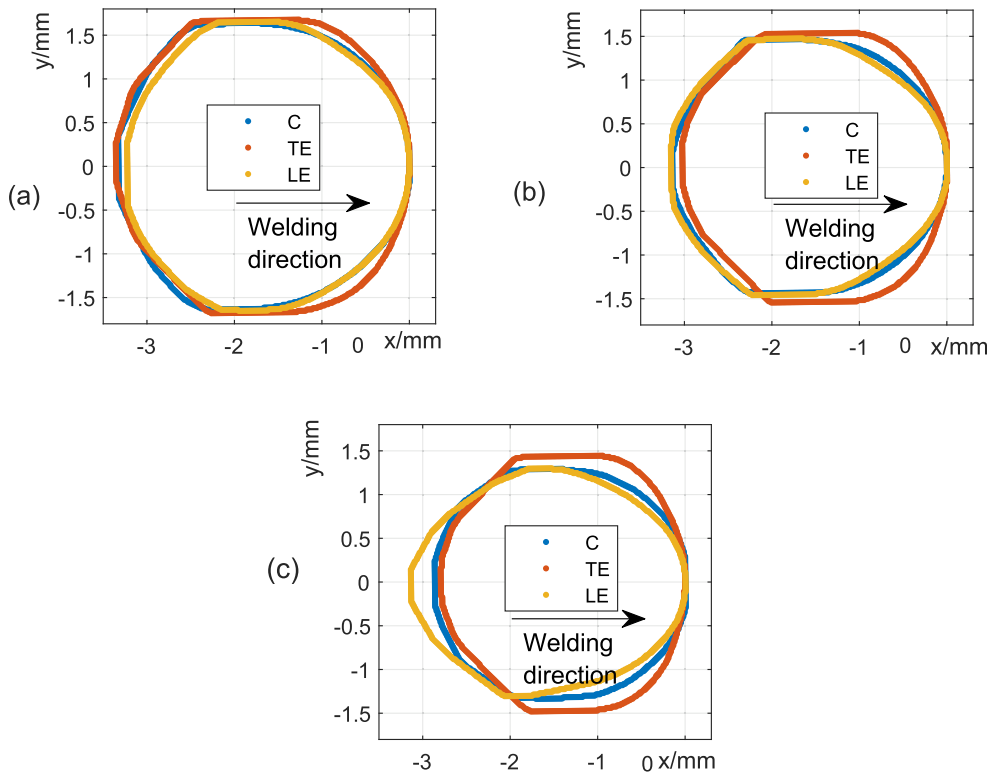
Fig. 6. Melt pool outer contours.

Fig. 7. Melt pool outer contours; (a): 5.0 mm/s, (b): 7.5 mm/s; (c): 10.0 mm/s.

mm/s. Comparing now the melt pool lengths obtained with the power density distributions C and LE, it is around 3% longer with LE when the travel speed is $U_{laser} = 7.5$ mm/s, and 7% longer when $U_{laser} = 10$ mm/s.

Fig. 9 shows for each case the time variation of the melt pool width. The coloured lines visualize the measurements in which outliers were replaced with the nearest element that is not an outlier. Outliers were defined as points outside three standard deviations from the mean. The black lines are the measurements filtered by a moving average filter with window size of 25 measurement points. More details about the

estimation procedure can be found in [32]. The plots of Fig. 9 confirm that the width measurements shown in Fig. 8a represent the trend all through the quasi-steady stage of the weldings.

3.2. Micrograph analysis

Micrographs of the welds obtained using the different power density distributions and travel speeds are shown in Fig. 10. It can be clearly seen that the welds processed at each power distribution i.e. C, TE and
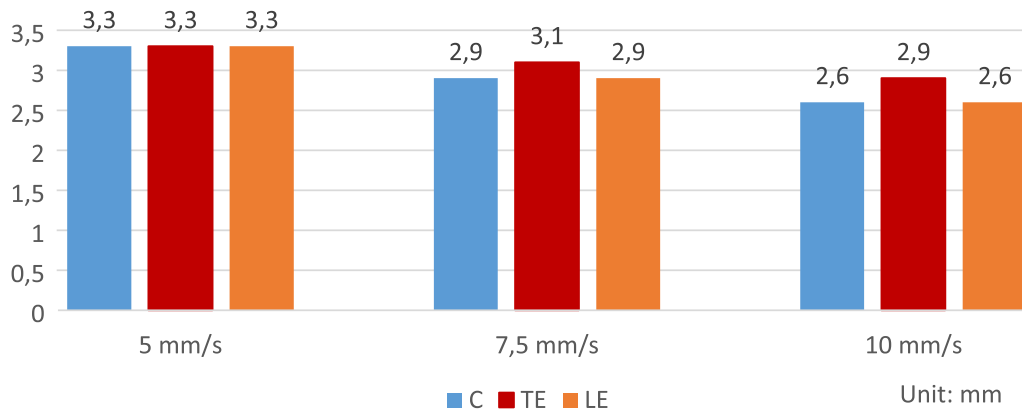
(a) Width
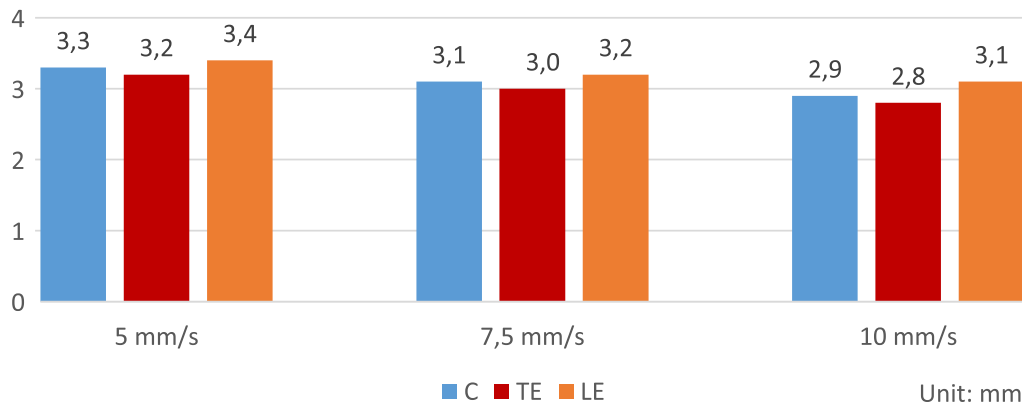
(b) Length
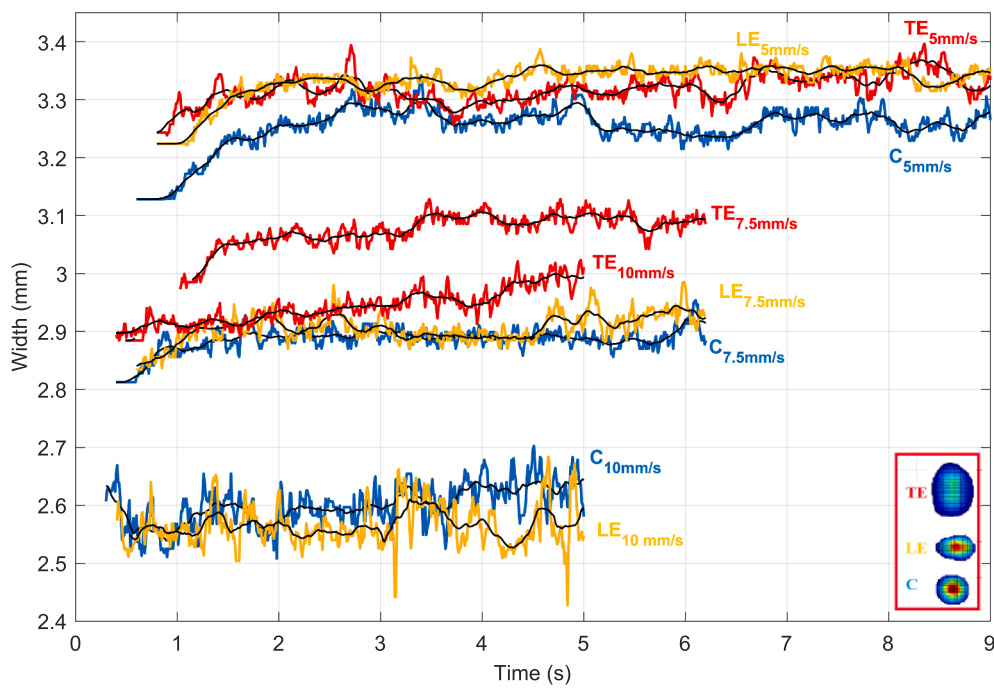
Fig. 8. Width and length of the melt pool.

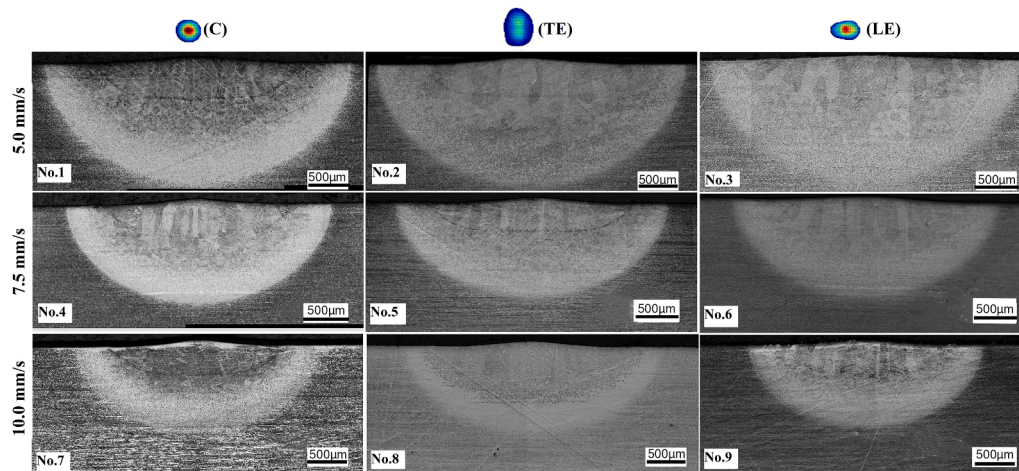**Fig. 9.** Time variation of the melt pool width.

Fig. 10. Cross sections from different power density distributions and different travel speeds.

LE, showed a decrease in FZ depth with an increase in the travel speed, which is expected. The weld width measured using optical micrographs at two different cross sections of each bead are listed in Fig. 11. The uncertainty of the reported measurements was evaluated to be $\pm$ 0.05 mm, which was determined by the standard deviation of the measurements. The source of error was attributed to the partially indistinct boundary between the HAZ and the FZ in certain cases. It can be seen that at the travel speed of 5.0 mm/s comparable width values that are around 3.3 mm were measured irrespective of the power density distribution. However, at the higher travel speeds of 7.5 and 10.0 mm/s, Fig. 11 clearly shows higher width of the FZ produced with the TE beam shape than with LE and C. In general, the phase constituents of Ti64 are a function of the thermal history (maximum temperature, cooling rates etc.), resulting in acicular α' (HCP) [33] or α(HCP)+β(BCC) [34,35]. Furthermore, the different microstructural features obtained in Ti64 are often refereed as globular α, Widmanstätten, martensitic, basketweave etc. [36]. SEM analysis was performed in order to examine the influence of different power density distributions on the microstructure at a given laser speed (10 mm/s). A schematic illustration of the laser welded specimen and the different regions (center of fusion zone [R1] and adjacent to HAZ [R2]) considered for microstructural analysis are shown in Fig. 12. The microstructure from R1 region of Ti64 specimens processed using different power distributions (C, TE and LE, respectively,) comprised the diffusion-controlled, Widmanstätten α (acicular) plates, see Fig. 13 (a, c, e, respectively). Similar microstructures comprising α-plates were reported for selective laser melting processed Ti64 specimens [37]. Furthermore, the prior β grain boundaries could also be seen in Fig. 13 (c). The α-plates in the TE specimen appear to be finer than the α-plates observed in C and LE specimens, see Fig. 13 (a, c and e). The reason can be attributed to relatively lower power density in TE than the C and LE specimens that enabled lower energy to be dissipated in the case of TE, resulting in finer α microstructure in TE. Ran et al. also

reported coarser α microstructure for higher energy input Ti64 specimens manufactured via Electron Beam Melting [38]. In the R2 region, massive α (α_m) microstructure along with martensitic (α') microstructure were observed in all the investigated specimens, see Fig. 13 (b, d, and f, respectively). In the past, Ahmed et al. [39] and Lu et al. [40] reported the formation of massive α (α_m) phase in Ti64 alloys that were processed utilizing Selective Electron Beam Melting (SEBM). It is reported that the formation of massive α (α_m) microstructure along with martensitic microstructure occurs at intermediate cooling rates (410–20 °C s^{-1}) whereas the diffusion controlled Widmanstätten α formation occurs at slower cooling rates (<20 °C s^{-1}). Furthermore, in this work, the α_m content decreased whereas the martensitic content increased in the microstructure for TE when compared to C and LE, See Fig. 13.

In general, during welding, faster cooling rates are expected at the fusion zone region adjacent to HAZ (heat affected zone) due to the high temperature gradient. On the other hand, slower cooling rates are expected at the center of fusion zone. This explains the formation of diffusion controlled-Widmanstätten α in the center of fusion zone due to slower cooling rates. On the other hand, faster cooling rates at region adjacent to HAZ led to the formation of α_m and martensitic microstructure. The difference in melt pool width, depth and microstructure of lower power density specimen (TE) compared to C and LE demonstrates the capability of different beam shapes to tailor the microstructure of Ti64 alloys.

3.3. Hardness testing

Fig. 14 shows the hardness profiles across the widths for all the investigated cases. The distance between two successive indents was 100 μm. The uncertainty of the next width measurements could thus be of the order of 0.2 mm. For the three cases (C, TE and LE) with welding
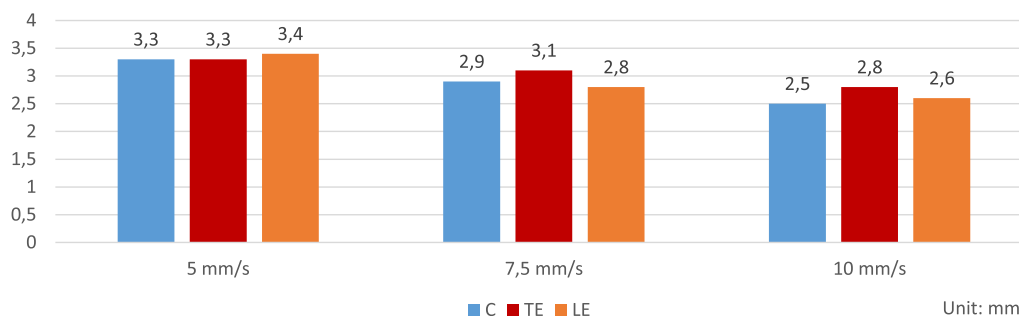

Fig. 11. FZ width of all the cases measured from microscopy images.
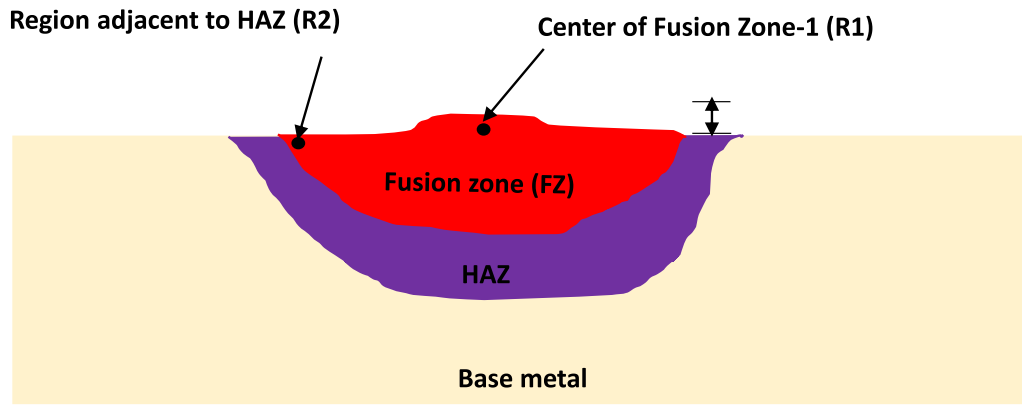
Fig. 12. Illustration of different regions (R1 and R2) of the weld considered for subsequent SEM analysis.
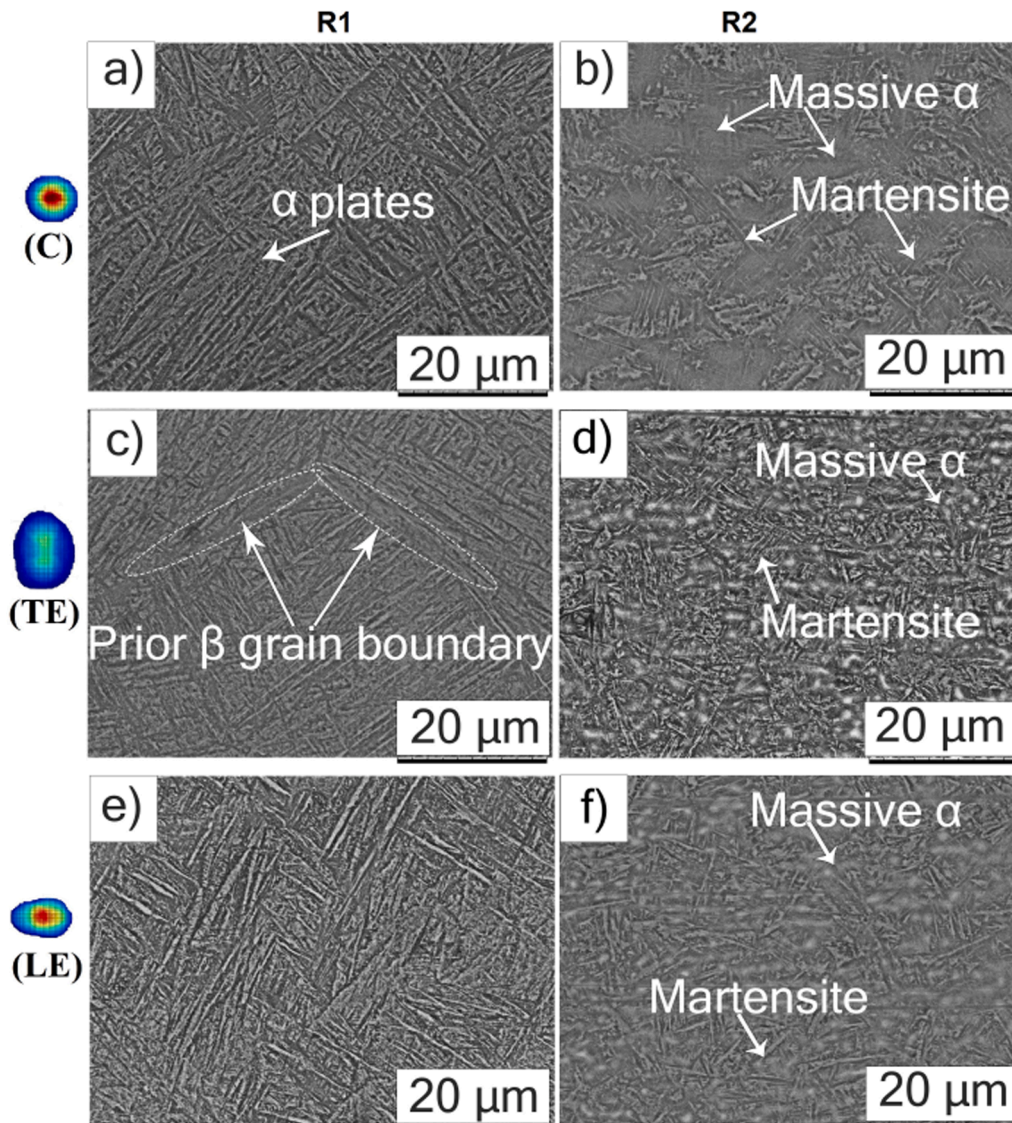

Fig. 13. SEM analysis for the regions R1 and R2 of Ti64 specimen processed at 10 mm/s laser travel speed utilizing different power density distributions C, TE and LE.

travel speed 10 mm/s, the widths of the FZ measured from the hardness profile are 2.7 mm, 3.1 mm and 2.9 mm, respectively. The width of the weld produced by laser beam with the TE profile was thus the widest. Fig. 15 shows the hardness profiles along the depth of the beads for all

the investigated cases. As can be seen in Figs. 14, 15 the hardness profile across the welds for all the investigated specimens showed consistently higher hardness (380 ± 15 HV0.5) for the FZ whereas the BM showed the lowest hardness values (315 ± 10 HV0.5). The hardness values for
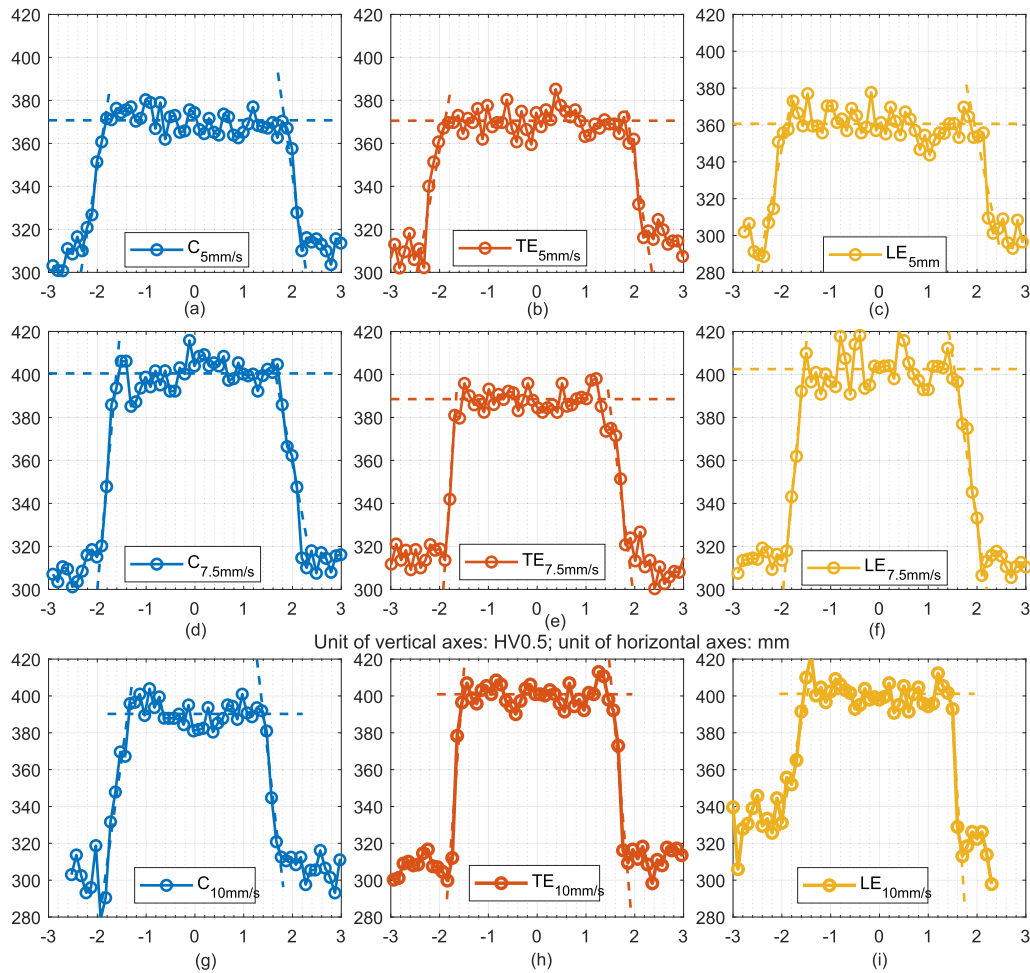
Fig. 14. Hardness profile along width direction for all the cases.

the FZ reported in this work were comparable to laser blown powder processed Ti64 reported elsewhere [36].

Fig. 16 visualizes the depth of the FZ measured from the hardness profiles. It is observed that, compared to distribution with C, at welding travel speed 5 mm/s and 7.5 mm/s, the LE shape produces welds that are around 7% and 9% deeper, respectively. Compared to distribution with C profile, at welding travel speed 7.5 mm/s and 10 mm/s, the TE shape produces welds that are around 9% and 10% shallower, respectively.

4. Discussion

The main objective of this work was to experimentally evaluate the performance of a new beam shaping technology and explore its potential to tailor the heat input and FZ in conduction mode LBW. The results of bead-on-plate welding experiments with Ti64 alloy show that by using a deformable mirror to shape the laser beam, the geometry of the melt pool can be modified. A wider, shorter and shallower melt pool or a narrower and longer melt pool can be obtained if TE or LE power density distributions are applied, respectively, compared to a C power distribution. This is in agreement with experimental findings presented by Ayoola et al. [10] and numerical study presented in [41]. The modification of the melt pool geometries is indicative of changes in melting and solidification behaviours as well as final weld properties. The melt pool width measured at the travel speed of 10 mm/s with the three different techniques used in this study (top view camera, microscopy and hardness profile) are compared in Fig. 17. It can be in seen that the different measurement methods lead to slightly different results. In particular the hardness results slightly overestimate (by 0.2 mm) the

width of the fusion zone, although these results do overlap when accounting for the measurement uncertainty. All the measurements reveal an identical trend with TE producing the widest welds.

It was observed in Fig. 7 that the melt pool geometries produced by the different beam profiles led to increasing differences when the travel speed was increased from 5.0 to 10.0 mm/s. This result suggests that for the process conditions of this study the effect of beam shaping on the melt pool is travel speed-dependent. Fig. 18 compares the evolution of the melt pool length and width (camera measurements) as a function of the travel speed for the three beam shapes. It can be seen that with the TE beam profile both width and length decrease linearly, and at the same rate, when the travel speed is increased from 5.0 to 10.0 mm/s. The proportions of the free surface contour are then preserved when the travel speed is changed. The length of the melt pool produced with the C beam shape presents also a linear evolution but not its width. Finally, with the LE beam shape the reduction in melt pool width and length lower, and they do it at different rates, as the travel speed is increased. Therefore the contours of the melt pool free surface produced with the C and LE beam shapes changed proportion when the travel speed was increases from 5.0 to 10.0 mm/s. On the other hand, considering now the depth to width ratio determined from the measurements at $U_{laser} = 10$ mm/s, the C, TE and LE profiles led to 0.37, 0.29, and 0.34, respectively. These ratio are all below the threshold value of 0.4 above which the welding regime is considered to change from conduction mode to transition mode [9]. The LE and C case are however rather close to this threshold. The depth to width ratio is expected to increase when the travel speed is decreased since the laser beam and material interaction time is then increased. The C and LE welds produced at lower travel
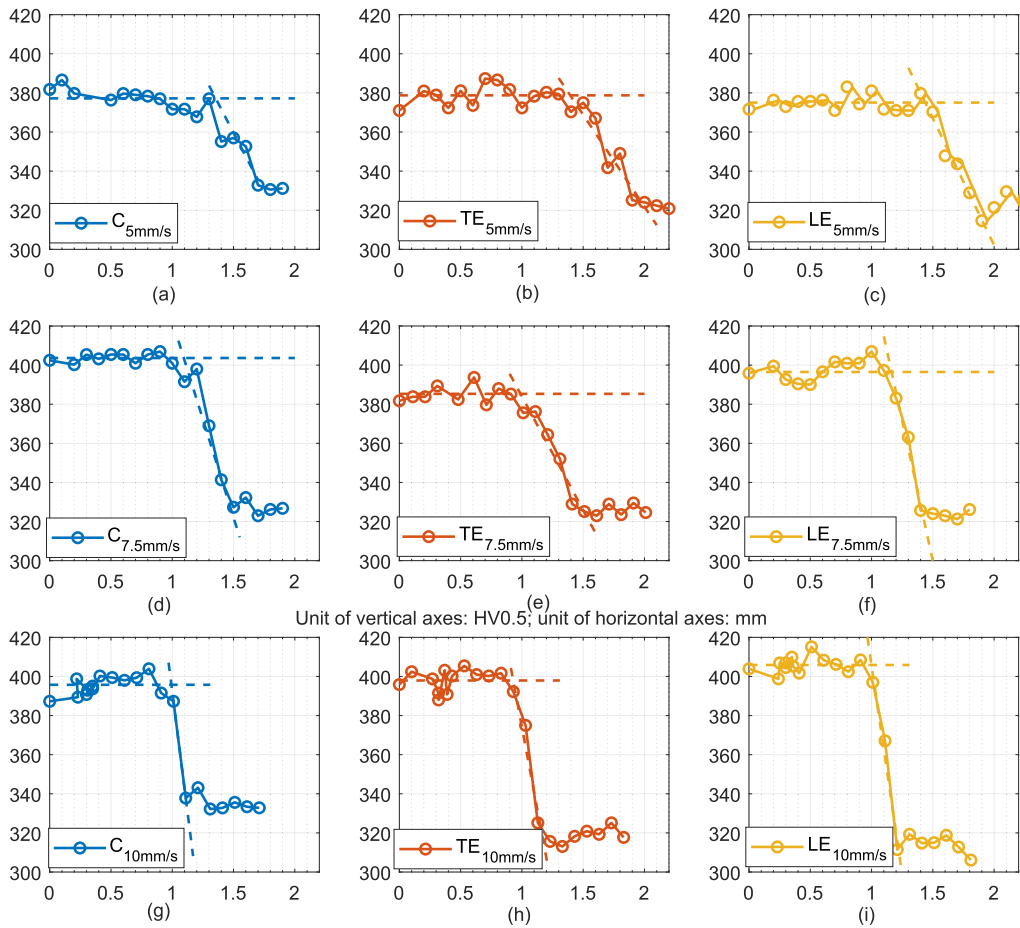
Fig. 15. Hardness profile along the depth direction for all the cases.
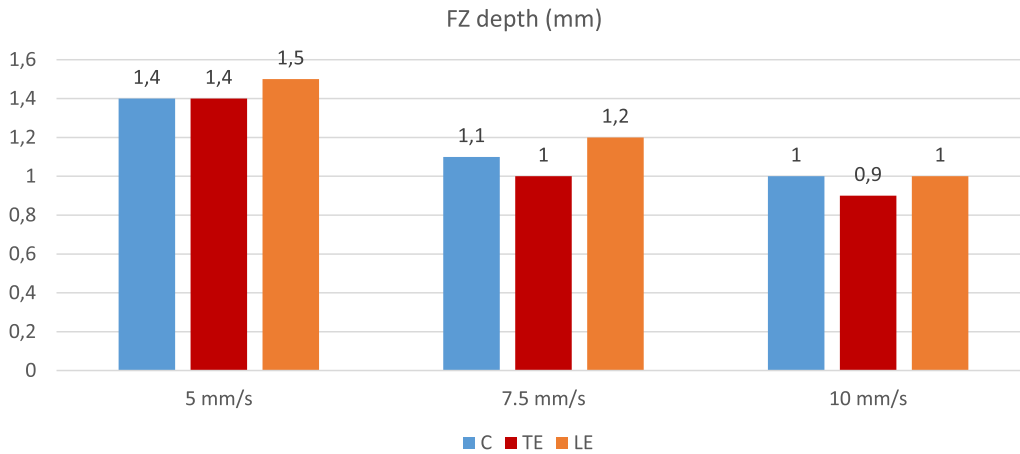

Fig. 16. Depth of FZ for all the investigated cases measured from hardness profile.

speed might therefore be in transition mode. This could be a source of change in melt pool geometry proportions. Another possible cause might be a change in flow pattern induced by the change in beam shape, as observed by Abadi et al. [41]. Further investigations would be needed to explore this question. This implies that the TE power density distribution might be a favourable option for LBAM, where a wider melt pool could improve process efficiency and the shallower melt pool reduces remelting of the previous layer.

5. Conclusions and future work

This work presents a deformable mirror system that enables beam shaping of multi-kilowatt cw fiber laser. Bead on plate conduction mode welding on Ti64 plates with three beam power distributions and three travel speeds has been performed to preliminarily evaluate this technology. The effect of the beam shaping on melt pool free surface geometry, cross section and hardness profiles were quantified.

Although the presented experimental work were conducted with cw laser power of 1 kW, the mirror has been tested with 2 kW cw power
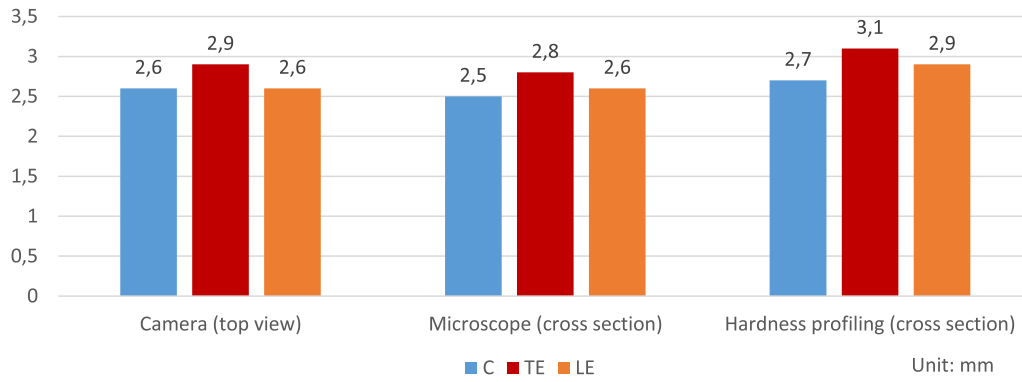
Fig. 17. Width measurement using different methods for 10.0 mm/s travel speed.
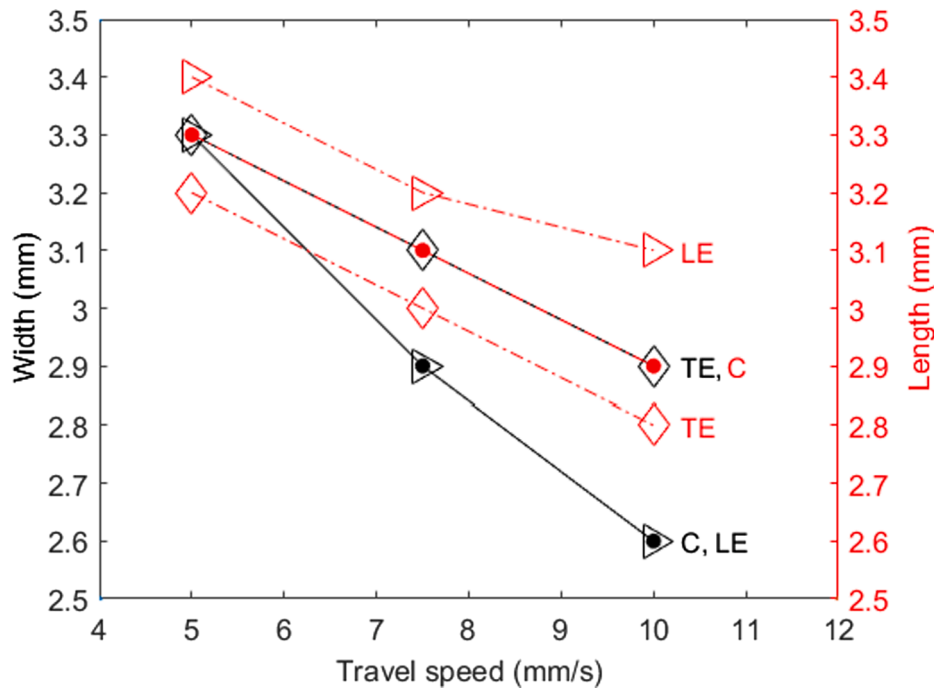

Fig. 18. Evolution of melt pool length and width with the travel speed.

during half an hour without any significant temperature rise on the mirror. In addition, the actuators of the deformable mirror were operated in half of the full working range, which means that there is potential to elongate the beam shape even more if needed. Moreover, the power distributions investigated were obtained by introducing only three aberration modes. In theory, the system can produce an infinite number of aberrations modes that make it possible to obtain a large number of different beam shapes. Based on these evaluations, the following conclusions can be drawn:

- Beam shaping using a deformable mirror can modify the melt pool geometries and the resulting FZ geometry and miscrostructure in conduction mode high power cw laser processing.
- At the travel speed $U_{laser} = 10.0$ mm/s, the produced melt pool width could be increased by around 12% and the depth reduced by 10% by applying a TE power distribution. The melt pool length could be increased by 7% without significant depth reduction by applying a LE power distribution.
- The deformable mirror system can operate at a frequency of 100 Hz, which offers the possibility to use it for adaptive control using sensors in closed loop even in fast dynamic processing.

- There is a huge potential in using this technology for control of LBW and LBAM processes that needs to be further explored.

Declaration of Competing Interest

The authors declare that they have no known competing financial interests or personal relationships that could have appeared to influence the work reported in this paper.

References

[1] G. Masinelli, T. Le-Quang, S. Zanoli, K. Wasmer, S.A. Shevchik, Adaptive laser welding control: A reinforcement learning approach, IEEE Access (2020).

[2] A. Konuk, R.G. Aarts, A. Huis, T. Sibillano, D. Rizzi, A. Ancona, et al., Process control of stainless steel laser welding using an optical spectroscopic sensor, Phys. Procedia 12 (2011) 744–751, https://doi.org/10.1016/j.phpro.2011.03.093.

[3] T. Sibillano, D. Rizzi, F.P. Mezzapesa, P.M. Lugarà, A.R. Konuk, R. Aarts, B.H. Veld, A. Ancona, et al., Closed loop control of penetration depth during co$_2$ laser lap welding processes, Sensors 12 (2012) 11077–11090, https://doi.org/10.3390/s120811077.

[4] H. Engström, A. Kaplan, Adaptive process control in laser robotic welding, in: Conference on Laser Materials Processing in the Nordic Countries: 04/08/2003-06/08/2003, Department of Geography, Norwegian University of Science and Technology, 2003, pp. 251–258.

[5] M. Nilsen, F. Sikström, A.-K. Christiansson, Adaptive control of the filler wire rate during laser beam welding of squared butt joints with varying gap width, Int. J. Adv. Manuf. Technol. 102 (2019) 3667–3676.

[6] A. Elefante, M. Nilsen, F. Sikström, A.-K. Christiansson, T. Maggipinto, A. Ancona, Detecting beam offsets in laser welding of closed-square-butt joints by wavelet analysis of an optical process signal, Opt. Laser Technol. 109 (2019) 178–185.

[7] S. Tolvanen, Microstructure and mechanical properties of ti-6al-4v welds produced with different processes, Department of Materials and Manufacturing Technology, Chalmers University Of Technology, Gothenburg, Sweden (2016).

[8] F.M. Dickey, L.S. Weichman, R.N. Shagam, Laser beam shaping techniques, in: High-Power Laser Ablation III, vol. 4065, International Society for Optics and Photonics, 2000, pp. 338–348.

[9] W. Ayoola, W. Suder, S.W. Williams, Parameters controlling weld bead profile in conduction laser welding, J. Mater. Process. Technol. 249 (2017) 522–530.

[10] W. Ayoola, W. Suder, S. Williams, Effect of beam shape and spatial energy distribution on weld bead geometry in conduction welding, Opt. Laser Technol. 117 (2019) 280–287.

[11] J.S. Rinne, S. Nothdurft, J. Hermsdorf, S. Kaierle, L. Overmeyer, Advantages of adjustable intensity profiles for laser beam welding of steel copper dissimilar joints, Procedia CIRP 94 (2020) 661–665.

[12] K. Hansen, F. Olsen, M. Kristiansen, O. Madsen, Joining of multiple sheets in a butt-joint configuration using single pass laser welding with multiple spots, J. Laser Appl. 27 (2015) 032011.

[13] M.J. Matthews, T.T. Roehling, S.A. Khairallah, G. Guss, S.Q. Wu, M.F. Crumb, J.D. Roehling, J.T. McKeown, Spatial modulation of laser sources for microstructural control of additively manufactured metals, Procedia CIRP 74 (2018) 607–610.

[14] T.T. Roehling, S.S. Wu, S.A. Khairallah, J.D. Roehling, S.S. Soezeri, M.F. Crumb, M.J. Matthews, Modulating laser intensity profile ellipticity for microstructural control during metal additive manufacturing, Acta Mater. 128 (2017) 197–206.

[15] A.S. Metel, M.M. Stebulyanin, S.V. Fedorov, A.A. Okunkova, Power density distribution for laser additive manufacturing (slm): potential, fundamentals and advanced applications, Technologies 7 (2019) 5.

[16] A. Mahrle, E. Beyer, Control of the energy deposition during laser beam welding by oscillation techniques, in: Proceedings of the 4th international WLT-conference on lasers in manufacturing, 2007, pp. 97–103.

[17] M. Kraetzsch, J. Standfuss, A. Klotzbach, J. Kaspar, B. Brenner, E. Beyer, Laser beam welding with high-frequency beam oscillation: welding of dissimilar materials with brilliant fiber lasers, in: International Congress on Applications of Lasers & Electro-Optics, volume 2011, Laser Institute of America, 2011, pp. 169–178.

[18] C. Thiel, A. Hess, R. Weber, T. Graf, Stabilization of laser welding processes by means of beam oscillation, in: Laser Sources and Applications, volume 8433, International Society for Optics and Photonics, 2012, p. 84330V.

[19] M. Schaefer, S. Kessler, P. Scheible, T. Graf, Modulation of the laser power to prevent hot cracking during laser welding of tempered steel, J. Laser Appl. 29 (2017) 042008.

[20] K. Hansen, M. Kristiansen, F. Olsen, Beam shaping to control of weldpool size in width and depth, Phys. Procedia 56 (2014) 467–476.

[21] J. Kell, J. Tyrer, R. Higginson, J. Jones, S. Noden, Laser weld pool management through diffractive holographic optics, Mater. Sci. Technol. 28 (2012) 354–363.

[22] B. Victor, S. Ream, C.T. Walters, Custom beam shaping for high-power fiber laser welding, in: International Congress on Applications of Lasers & Electro-Optics, volume 2008, Laser Institute of America, 2008, p. 1301.

[23] S. Feuchtenbeiner, W. Dubitzky, T. Hesse, N. Speker, P. Haug, J. Seebach, J.-P. Hermani, D. Havrilla, Beam shaping brightline weld: latest application results, in: High-Power Laser Materials Processing: Applications, Diagnostics, and Systems VIII, vol. 10911, International Society for Optics and Photonics, 2019, p. 109110X.

[24] L. Mrňa, M. Šarbort, Š. Řeřucha, P. Jedlička, Feedback control of laser welding based on frequency analysis of light emissions and adaptive beam shaping, Phys. Procedia 39 (2012) 784–791.

[25] L. Mrňa, M. Šarbort, Š. Řeřucha, P. Jedlička, Adaptive optics for control of the laser welding process, in: EPJ Web of Conferences, vol. 48, EDP Sciences, 2013, p. 00017.

[26] V. Samarkin, A. Alexandrov, V. Toporovsky, A. Rukosuev, A. Kudryashov, Water-cooled deformable mirrors for high power beam correction, in: Fourth International Symposium on High Power Laser Science and Engineering (HPLSE 2021), vol. 11849, International Society for Optics and Photonics, 2021, p. 1184917. https://doi.org/10.1117/12.2599116.

[27] A.N. Lylova, Y.V. Sheldakova, A.V. Kudryashov, V.V. Samarkin, Formation of doughnut and super-gaussian intensity distributions of laser radiation in the far field using a bimorph mirror, Quant. Electron. 48 (2018) 57.

[28] R.K. Tyson, Introduction to adaptive optics, vol. 41, SPIE Press, 2000.

[29] J. Mocci, M. Quintavalla, C. Trestino, S. Bonora, R. Muradore, A multiplatform cpu-based architecture for cost-effective adaptive optics systems, IEEE Trans. Ind. Informat. 14 (2018) 4431–4439, https://doi.org/10.1109/TII.2018.2799874.

[30] Z. Zhang, A flexible new technique for camera calibration, IEEE Trans. Pattern Analysis Mach. Intell. 22 (2000) 1330–1334.

[31] S. Bloom, E. Korevaar, J. Schuster, H. Willebrand, Understanding the performance of free-space optics, J. Opt. Netw. 2 (2003) 178–200.

[32] Y. Mi, S.M.A. Noori Rahim Abadi, F. Sikström, I. Choquet, A. Ancona, Dynamic free surface contour measurement of the melt pool applied to conduction laser beam welding of Ti-6Al-4V and model evaluation, 2021. (preprint in ISBN: 978-91-88847-96-6).

[33] L. Thijs, F. Verhaeghe, T. Craeghs, J. Van Humbeeck, J.-P. Kruth, A study of the microstructural evolution during selective laser melting of ti–6al–4v, Acta Mater. 58 (2010) 3303–3312.

[34] M. Simonelli, Y.Y. Tse, C. Tuck, The formation of $\alpha+\beta$ microstructure in as-fabricated selective laser melting of ti-6al-4v, J. Mater. Res. 29 (2014) 2028.

[35] D. Banerjee, J. Williams, Perspectives on titanium science and technology, Acta Mater. 61 (2013) 844–879.

[36] M. Neikter, P. Åkerfeldt, R. Pederson, M.-L. Antti, V. Sandell, Microstructural characterization and comparison of ti-6al-4v manufactured with different additive manufacturing processes, Mater. Characteriz. 143 (2018) 68–75.

[37] B. Wysocki, P. Maj, R. Sitek, J. Buhagiar, K.J. Kurzydlowski, W. Święszkowski, Laser and electron beam additive manufacturing methods of fabricating titanium bone implants, Appl. Sci. 7 (2017) 657.

[38] J. Ran, F. Jiang, X. Sun, Z. Chen, C. Tian, H. Zhao, Microstructure and mechanical properties of ti-6al-4v fabricated by electron beam melting, Crystals 10 (2020), https://doi.org/10.3390/cryst10110972. URL: https://www.mdpi.com/2073-4352/10/11/972.

[39] T. Ahmed, H. Rack, Phase transformations during cooling in $\alpha+\beta$ titanium alloys, Mater. Sci. Eng. A 243 (1998) 206–211.

[40] S. Lu, M. Qian, H. Tang, M. Yan, J. Wang, D. StJohn, Massive transformation in ti–6al–4v additively manufactured by selective electron beam melting, Acta Mater. 104 (2016) 303–311.

[41] S.N.R. Abadi, Y. Mi, F. Sikström, A. Ancona, I. Choquet, Effect of shaped laser beam profiles on melt flow dynamics in conduction mode welding, Int. J. Therm. Sci. 166 (2021) 106957.